Volume 16, Issue 3, 162519 (1-13)

International Journal of Nano Dimension (IJND)

https://dx.doi.org/10.57647/j.ijnd.2025.1603.19

IR gold-coated circular photonic crystal fiber surface plasmon resonance (C-PCF-SPR) sensor

Maryam Mirasanloo Zeydi[1], Seyed Saleh Ghoreishi Amiri[1,*], Reza Yousefi[1], Habib Aderang[2]

[1]*Department of Electrical Engineering, No.C., Islamic Azad University, Noor, Iran.*
[2]*Department of Electrical Engineering, Faculty of Engineering and Technology, University of Mazandaran, Babolsar, Iran.*

[*]**Corresponding author:** ss.ghoreishi@iau.ac.ir

Original Research

Received:
29 September 2024
Revised:
17 December 2024
Accepted:
18 December 2024
Published online:
1 June 2025

Abstract:

Wavelength and amplitude sensitivities are crucial aspects in optimizing the performance of photonic crystal fiber sensors. This study presents a novel approach to enhance sensitivity by designing a circular photonic crystal fiber-based surface plasmon resonance (C-PCF-SPR) sensor. The proposed sensor is characterized by three central air holes and a thin gold coating serving as the plasmonic medium, allowing it to achieve resonance wavelengths in the infrared range (3000 to 3300 nm). The sensor's propagation characteristics were evaluated using the finite difference eigenmode solver method via Lumerical software. Within a refractive index (RI) interval of 1.34 to 1.38, the sensor demonstrated a maximum wavelength sensitivity of 18681 nm/RIU and an amplitude sensitivity of 942.47 RIU^{-1}. The sensor's resolution reaches up to 1×10^{-4} RIU, with a figure of merit (FOM) calculated to be 311.35 RIU^{-1} in the same RI range. Given its structural similarity to conventional PCFs, the sensor is expected to be highly feasible for real-world applications. Furthermore, numerical analysis suggests that the sensor can effectively detect various blood components, including plasma, white blood cells (WBCs), hemoglobin (Hb), ethanol, and captone, as well as distinguish between healthy and cancerous cells, with an optimal gold layer thickness of 0.1 μm.

Keywords: Plasmonic; Refractive index (RI); Sensor; Signal-to-Noise ratio (SNR); Single mode fiber (SMF)

1. Introduction

Biosensors are poised to play a crucial role across various domains such as food safety, biochemical technologies, medicine, and everyday applications. Sensors that utilize surface plasmon resonance (SPR) for high sensitivity to gas and biological signals [1–3], as well as micro-ring resonators, have been investigated. Surface plasmon sensors were predominantly designed using Kretschmann prism configurations, which rely on the principle of total internal reflection. However, these prism-based SPR sensors face limitations such as their bulkiness and the presence of multiple optical and mechanical components, which complicate their use in remote sensing applications [4]. To address some of these limitations, including remote sensing, there has been a shift towards optical fibers. Among these, photonic crystal fibers (PCFs) are particularly notable for their versatility, compact size, tunability, and suitability for remote sensing applications [5–8].

A notable advancement was the circular PCF-SPR sensor with a wide detection range [9]. Unlike later designs that coated the inner or outer surfaces of the air holes with a thin metal film, this design utilized air holes filled with gold metal. Additionally, another PCF-SPR design was introduced that involved coating both sides, demonstrating significantly greater sensitivity compared to sensors coated on only one side [10]. These internal sensing PCF-SPR sensors with internal sensing capabilities have advanced significantly. The manufacture of these internal sensing PCF-SPR sensors is often complex, particularly when it comes to filling air holes with gold or depositing gold films on the surfaces. External sensing capability sensors offer a solution to these challenges [11–14]. In 2019, a PCF-SPR sensor was introduced using titanium nitride (TiN) as a coating material [11]. TiN is favored for SPR sensors due to its exceptional properties, including a high melting point and chemical stability [11]. In another study, a new PCF-SPR structure was developed that incorporated a thin TiO_2 film between the fiber and the plasmonic material, leading to enhanced sensitivity [12].

In reference [13], a new high-sensitivity gold-coated PCF-SPR sensor with excellent structural compatibility was explored. Additionally, another PCF-SPR sensor with a wide frequency range was introduced using indium tin oxide (ITO) [14]. To address the challenges of coating plasmonic materials on the inner surfaces of air holes and selectively impregnating analyte materials, PCF-SPR sensors with D-shaped configurations have been developed [5] and [15–19]. In 2019, a PCF sensor with a D-shaped configuration was introduced, offering a wide refractive index (RI) detection range. This sensor achieved maximum sensitivities of 7900 nm/RIU and 5300 nm/RIU using analyte layers with thicknesses of 1,500 nm and 500 nm, respectively [5]. A double coating of indium tin oxide (ITO) and zinc oxide (ZnO) was proposed as an alternative to traditional plasmonic materials in another design for a D-shaped PCF-SPR sensor [15]. In this design, the SPR frequency is tuned by adjusting the metal-to-oxygen concentration ratio [15]. Another D-shaped PCF-SPR sensor was developed with a stack consisting of a TiO_2 thin film, a gold layer, and a graphene thin film on the surface of the fiber. This design offers high sensitivity and a wide wavelength detection range [16]. Other D-shaped PCF-SPR sensor structures include those utilizing titanium nitride as the plasmonic material [17], incorporating a graphene layer over a gold film [18], and featuring two external sensing passageways near the polished surface [19].

In recent years, the development of photonic crystal fiber-based surface plasmon resonance (PCF-SPR) sensors has seen significant advancements. However, many designs face challenges related to fabrication complexity, limited detection ranges, or suboptimal sensitivity. Our study introduces a novel C-PCF-SPR sensor design that emphasizes simplicity and practicality while maintaining high sensitivity. Unlike traditional designs requiring intricate internal modifications or alternative plasmonic materials, our sensor achieves competitive performance using a straightforward gold-coated external sensing mechanism. This balance of performance and manufacturability addresses key gaps in the field and enables broader adoption of the technology.

This study presents a new circular PCF-SPR (C-PCF-SPR) sensor with external sensing capabilities. The propagation properties of this sensor are analyzed using Lumerical software, and the effects of varying structural parameters on the sensor's performance are explored. This article highlights a C-PCF-SPR sensor with a structure closely resembling that of a conventional photonic crystal fiber. Unlike previous sensors, which involved complex manufacturing processes to alter the PCF structure, this new design maintains the original PCF structure while achieving high sensitivity and performance. The C-PCF-SPR sensor simplifies the manufacturing process by avoiding the need for gold layer deposition on internal surfaces or extensive polishing, as seen in earlier designs. The sensor shows exceptional performance within an RI range of $1.34 - 1.38$, achieving maximum wavelength and amplitude sensitivities of 18,7 nm/RIU and 942 RIU^{-1}, respectively, in this range. This makes it a cost-effective and time-efficient alternative for conventional detection techniques used in diagnosing various blood components [20–23]. Additionally, the sensor can distinguish between healthy and cancerous cells with a gold layer thickness of 0.1 μm [24–27].

The paper is organized into four sections. Section 2 of the paper provides an in-depth discussion of the proposed structure, its design considerations, and the simulation method. The simulation results and analysis and comparison with previous structure are presented in section 3 and finally, section 4 concludes the paper.

2. Structure and principle

The 2D cross-section x-y view, the corresponding 3D and the x-z view of the designed C-PCF-SPR sensor with three central air holes are shown in Fig. 1 (a), (b) and (c), respectively. The biosensor structure is composed of three central circular air holes, enclosed by four concentric rings of circular air cavities embedded in a high-purity silica fiber. The second layer of the structure includes a gold layer that functions as the plasmonically active medium, while the next layer contains a channel for the analyte.

This specific structure and design of the C-PCF-SPR sensor, were developed by leveraging findings from a previous study [28]. The referenced study focused on designing an improved photonic crystal fiber aimed at minimizing losses and scattering. However, for the purpose of enhancing the SPR effect, we selected a design that intentionally exhibits higher losses. This choice was made to facilitate the guidance of light towards the cladding and to enhance the surface plasmon resonance phenomenon by ensuring that light interacts effectively at the metal-dielectric interface. The increased losses contribute to amplifying the SPR effect, which is crucial for the sensor's sensitivity and performance.

In the suggested structure, the three central air holes each have a radius of 0.7 μm. The air holes in the second ring also measure 0.7 μm in radius, whereas those in the outer rings are smaller, with a radius of 0.4 μm. The pitch, defined as the spacing between the centers of two adjacent holes, is 2.2 μm. The analyte layer has a thickness of 0.9 μm, while the gold layer, serving as the active plasmonic material, is 0.05 μm thick. The refractive index (RI) of the analyte ranges from 1.34 to 1.38, enabling effective sensing throughout this interval.

This specific configuration is designed to optimize the sensor's performance by carefully balancing the dimensions of the air holes, the pitch and the gold and analyte layers thicknesses to enhance the surface plasmon resonance effect and improve the sensor's sensitivity.

Figure 1 (d) illustrates the measurement system setup designed to evaluate the feasibility of the proposed sensor. In this configuration, a light source with a broad spectrum (DH-2000-BAL, Ocean Optics Inc.) is directed through a single-mode fiber (SMF) to the D-shaped PCF-SPR sensor region, where the SPR effect is excited.

Once the SPR effect is triggered, a second SMF is used to couple the sensing head to a miniature spectrometer (USB 4000, Ocean Optics Inc.). The spectrometer detects changes in the loss spectrum, which are influenced by changes in the temperature of the external analyte around the sensor

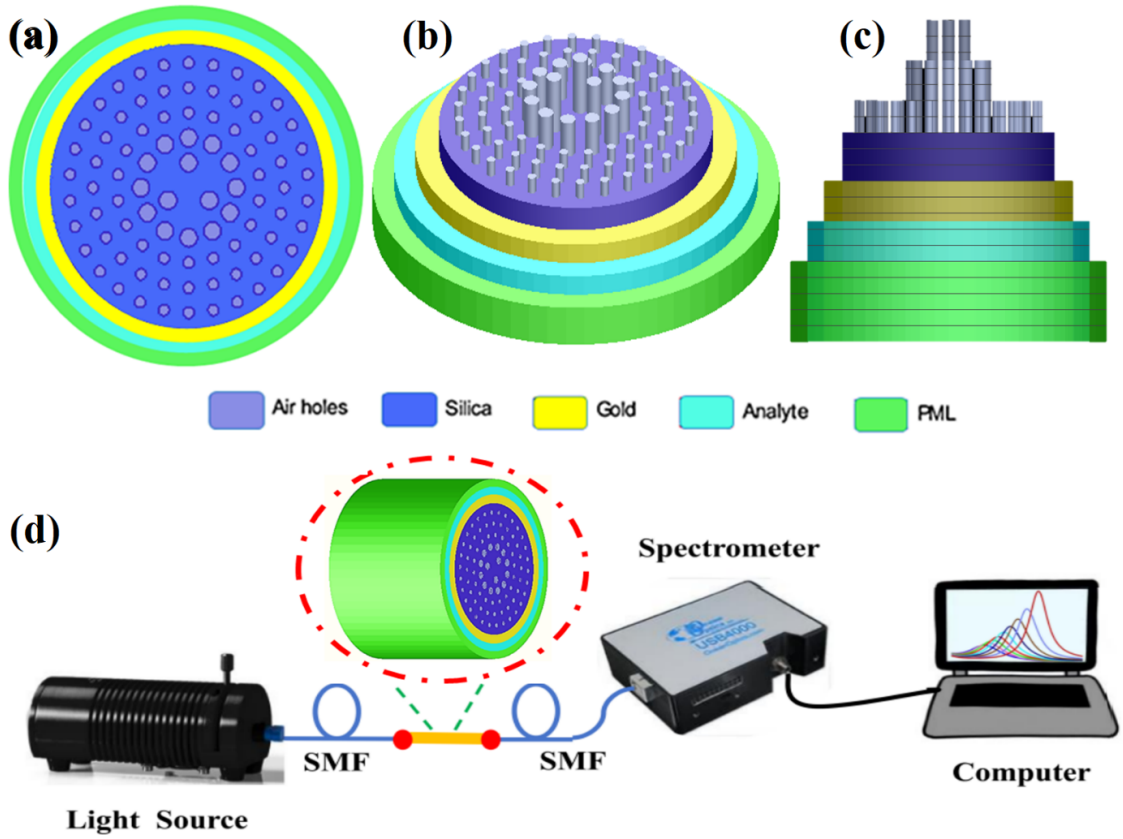

Figure 1. Structural schematic of (a) 2D cross-section x-y view, (b) the corresponding 3D and (c) the x-z view of the designed C-PCF-SPR sensor with three central air holes. (d) Measurement system setup of the C-PCF-SPR sensor with three central air holes.

and the refractive index (RI). The collected spectral data is then transmitted to a computer, where it undergoes further analysis to determine the sensor's performance and sensitivity. This setup allows for precise monitoring and analysis of how the D-type PCF-SPR sensor responds to changes in its environment, validating its effectiveness for practical applications [29].

To evaluate the performance characteristics of the proposed biosensor, the finite difference eigenmode (FDE) method has been applied using Lumerical software. This method calculates the spatial properties and frequency response of the modes by solving Maxwell's equations over the cross-sectional mesh of the PCF. The FDE method is capable of determining state field profiles, effective indices, and losses associated with the modes.

The solver utilizes a Cartesian-style rectangular mesh, where each basic simulation quantity such as material properties, geometric details, and electric and magnetic fields is calculated at every point on the mesh. Although a finer mesh offers a more precise representation of the device, it significantly increases time, memory demands, and computational cost. The MODE solver offers a consistent meshing algorithm that provides precise outcomes even with comparatively coarse meshing. After meshing the structure, sparse matrix techniques have been used to solve the eigenvalue problem matrix. Effective refractive index of the waveguide modes and the corresponding mode profiles have been extracted through this approach. The method employed in this analysis is based on the approach originally developed by Zhu and Brown, with certain modifications and enhancements tailored to this specific application [30].

In the following the wave vector equation, which underpins this analysis, is presented below:

$$\nabla \times ([S]^{-1} \nabla \times E) - k_0^2 n^2 E = 0 \tag{1}$$

where E is the electric field vector, $k_0 = \frac{2\pi}{\lambda_0}$ is the vacuum wave number, n is the domain RI, S is a 3×3 PML matrix, $[S]^{-1}$ represents the inverse matrix and λ_0 is the operating wavelength.

β is the propagation constant which is calculated as equation (2). It indicates the phase rotation per unit length [31, 32].

$$\beta = n_{eff} k_0 = \frac{2\pi}{\lambda_0} n_{eff} = \frac{2\pi}{\frac{\lambda_0}{n_{eff}}} = \frac{2\pi}{\lambda_{eff}} \tag{2}$$

n_{eff} and λ_{eff} represent the mode of RI and the conduction wavelength in the medium, respectively.

A surface plasmon wave (SPW) is an electromagnetic wave that propagates at the metal-dielectric interface. The SPW propagation constant is obtained by the equation (3) [9]:

$$\beta_{\mathrm{SPW}} = \frac{\omega}{c} \sqrt{\frac{\varepsilon_m \varepsilon}{\varepsilon_m + \varepsilon_d}} \tag{3}$$

In the wave vector equation referenced above (Eq. (3)), the speed of light in a vacuum, the angular frequency of the electromagnetic wave, and the dielectric constants of the

metal and dielectric material are denoted by c, ω, ε_m, and ε_d, respectively. These parameters are crucial in determining the behavior of the wave as it propagates through the photonic crystal fiber, particularly in the context of (SPR) where the interaction between the metal-dielectric interface and the electromagnetic wave is crucial for the sensor's sensitivity and overall performance. PCF-based plasmonic sensors operate by leveraging the interaction of light with the damping fields on the metal surface. By injecting light into the core of the PCF, a damping field is generated and extends into the cladding region (metal surface).

At the resonance condition, a loss peak is observed in the transmission spectrum. This loss peak arises because the plasmonic mode effectively couples with the core mode, resulting in energy being absorbed by the metal surface. The shift in the position of this loss peak occurs as the refractive index of the surrounding analyte changes. By monitoring these shifts, the sensor can detect changes in the refractive index of the analyte, allowing for the identification and quantification of different substances [13].

The confinement loss (CL) of PCFs is calculated using the imaginary part of the effective RI as equation (4) [33]:

$$\mathrm{CL} = 40\pi \frac{\mathrm{Im}(n_{eff})}{\ln(10)\lambda} \frac{dB}{m} \tag{4}$$

In the above equation, $\mathrm{Im}(n_{eff})$ is the imaginary part of the effective refractive index of the core and λ represents the free-space wavelength in meter.

Equation (5) shows the silica RI using the Sellmeier equation [13]:

$$n^2(\lambda) = 1 + \frac{B_1\lambda^2}{\lambda^2 - C_1} + \frac{B_2\lambda^2}{\lambda^2 - C_2} + \frac{B_3\lambda^2}{\lambda^2 - C_3} \tag{5}$$

where $B_1 - B_3$ and $C_1 - C_3$ are the Sellmeier coefficients, λ is the wavelength (μm) and n is the refractive index of the silica fiber. ($C_1 = 4.67914826 \times 10^{-3}$ $\mu\mathrm{m}^2$, $C_2 = 1.35120631 \times 10^{-2}$ $\mu\mathrm{m}^2$ and $C_3 = 97.9340025$ $\mu\mathrm{m}^2$, $B_1 = 0.69616300$, $B_2 = 0.407942600$, $B_3 = 0.897479400$).

The permittivity coefficient of the gold is calculated by the equation (6) (Drude equation), which provides a model for the dielectric function of metals like gold. The equation takes into account both free electron contributions and bound electron contributions to the permittivity.

ω and ε_∞ = 5.967 and c represents the angular frequency, coefficient of the high-frequency permittivity and the light speed in a vacuum, respectively. $\frac{\Gamma_l}{2\pi} = 104.86$ THz and $\frac{\Omega_L}{2\pi} = 650.07$ THz are the spectral width and resonant frequency of the Lorentz oscillator and $\gamma_D/2\pi = 15.92$ THz and $\omega_D/2\pi = 2113.6$ THz denote the plasma and damping frequency. $\Delta\varepsilon$ is the balance factor which is 1.09 [13].

$$\varepsilon_{Au} = \varepsilon_\infty - \frac{\omega_D^2}{\omega(\omega + j\gamma_D)} - \frac{\Delta\varepsilon.\Omega_L^2}{(\omega^2 - \Omega_L^2) - j\Gamma_l\omega} \tag{6}$$

This detailed model is crucial for accurately predicting the optical properties of gold, particularly in the context of plasmonic sensors, where the interaction between light and the metal surface plays a pivotal role in sensor performance.

3. Results and discussion

3.1 Coupling characteristics analysis

The performance of the proposed sensor relies heavily on the excitation of damping fields and the effective interaction of light with the metal surface. At specific wavelengths, these damping fields interact with the metal surface to produce resonance phenomena. Figures 2 (a) and 2 (b) depict the electric field profile at the at a refractive index of $n = 1.37$, for the core's fundamental and the SPP mode, respectively. By introducing light into the core at an angle greater than the critical angle, it is reflected off the metal layer that divides the high refractive index (RI) core of the fiber from the surrounding analyte channels in the PCF. This reflection results in the generation of a damping field between the dielectric medium and the metal layer. The interaction of this damping field with the metal layer creates surface plasmon waves, as shown in Figure 2 (b).

In Fig. 3, the performance of the proposed structure has been investigated by analyzing the real part of the effective RI of both the plasmonic and the core mode (34 and 31), along with the loss peak of the fundamental mode when the refractive index $n = 1.37$. This analysis is crucial for understanding the SPR effect within the sensor. At a specific wavelength of 3.09677 μm, both of them are equal,

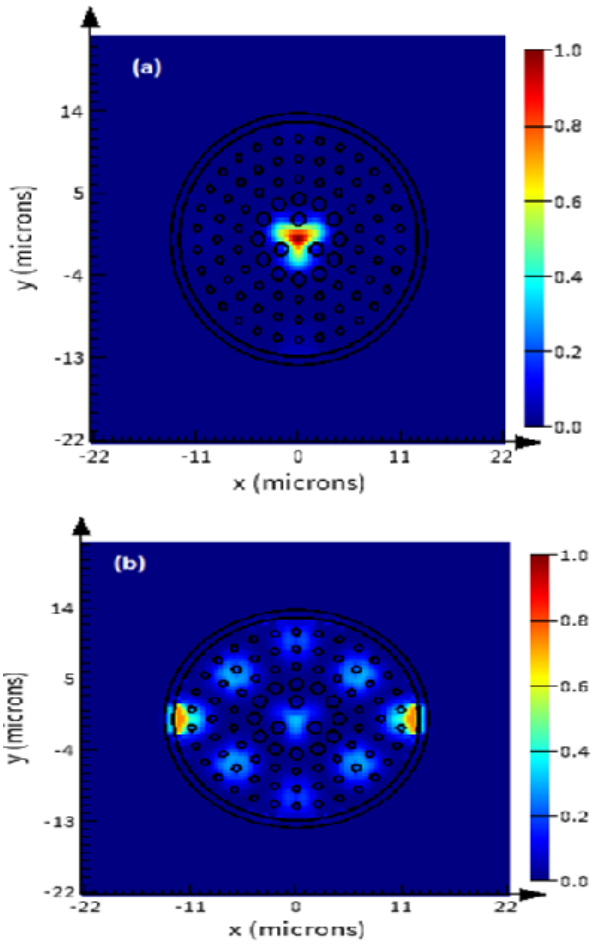

Figure 2. Electric field profile at the refractive index n = 1.37; (a) Core mode 31, (b) SPP mode 34 of the C-PCF-SPR sensor with three central air holes.

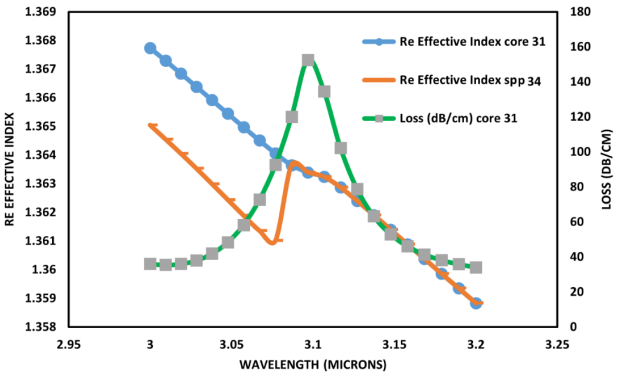

Figure 3. Loss spectra with the dispersion relation of core-guided mode and SPP mode at the refractive index n = 1.37. The real part of the fundamental mode (blue), plasmon mode (red) and imaginary part of the fundamental mode (losses) (green line).

with Real Neffcore = Real Neffspp = 1.3634. This equality confirms the phase matching condition and as results the occurrence of SPR. At the wavelength of 3.09677 μm, the loss spectrum exhibits a sharp peak with a loss value of 152.512 dB/cm. This sharp loss peak corresponds to the maximum transmission power and indicates a strong coupling between the core mode and the surface plasmon mode. The sharp loss peak observed at the resonance wavelength is due to the difference in RI between the core and the metal coating, further confirming the occurrence of SPR.

Figure 4 illustrates the confinement loss spectrum for different refractive indices (RIs) of the analyte, ranging from 1.34 to 1.38 with increments of 0.01. This spectrum is critical for understanding the behavior of the C-PCF-SPR sensor as it interacts with analytes of varying RIs.

The loss spectrum reveals that each analyte with a different RI causes the plasmonic mode to exhibit a distinct refractive index. This variation in the plasmonic mode's refractive index leads to a coupling with the core's fundamental conduction mode at different wavelengths, resulting in loss peaks at those wavelengths. With an increase in the refractive index (RI) from 1.34 to 1.38, the loss peak shifts to longer wavelengths, exhibiting a noticeable red shift. This shift is indicative of the sensor's sensitivity variations in the refractive index (RI) of the external environment. The trend

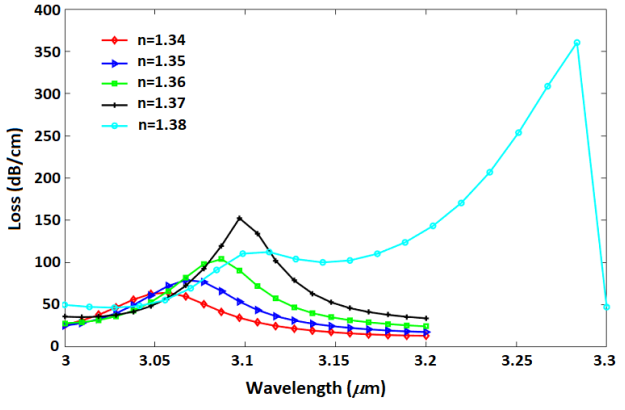

Figure 4. Loss spectrum of C-PCF-SPR for analyte RI varying from 1.34 to 1.38.

observed in the spectrum shows a gradual red-shift in the resonance wavelength as the RI increases. This red-shift corresponds to the sensor's response to higher RIs, where the resonance condition (and thus the loss peak) occurs at longer wavelengths. Additionally, as the RI increases, there is a noticeable increase in the magnitude of the loss peak. This indicates a stronger coupling between the SPP mode and the core's fundamental mode at higher refractive indices.

At an RI of 1.34, the loss peak occurs at a wavelength of 3057.32 nm, with a relatively low peak loss of 64.48 dB/cm. This suggests weaker coupling at this lower RI. In contrast, at an RI of 1.38, the loss peak shifts to a wavelength of 3283.58 nm with a significantly higher peak loss of 360.386 dB/cm. This reflects the most significant coupling (strongest) between the core mode and the SPP mode which leads to the highest observed loss.

3.2 Influence on sensing characteristics of structural parameters

In this section, we assess the effect of different parameters on the performance of the proposed design. The variables being considered include the plasmonic material type, thickness of the metal layer (t) and the radius of the air holes (r). To systematically analyze the impact of each variable on the performance of the suggested design, the control variable method is employed. This approach allows for precise monitoring of changes in the loss spectrum by varying one parameter at a time while keeping all other parameters constant.

3.2.1 Optimization of gold film thickness (t)

The impact of the thickness of the gold plasmonic material on the sensor's performance has been extensively examined, as illustrated in Figs. 5 (a) and 5 (b). This investigation highlights the critical role that the gold layer thickness plays in determining the sensor's sensitivity and resonance characteristics. The study reveals that increasing the thickness of the gold layer at a constant RI induces a blueshift in the resonance wavelength and simultaneously reduces the loss value. This blue-shift indicates a shift towards shorter wavelengths as the thickness increases. However, this comes at the cost of a decreased sensitivity, as evidenced by the loss value reduction. Specifically, a gold film with a thickness of 0.05 μm yields the sharpest resonance peak, characterized by the narrowest Full Width at Half Maximum (FWHM). This sharp peak signifies a high-quality resonance with strong sensitivity to RI changes. In contrast, a thicker gold layer of 0.15 μm results in a flatter peak with a wider FWHM, which could compromise the sensor's performance. The wider FWHM suggests diminished resonance quality, which can lead to false positives in detection, as the SPR effect becomes less pronounced when the metal layer is too thick for the electric field to penetrate effectively.

To further evaluate the impact of the thickness of the gold on the sensor's sensing functionality, Fig. 5 (b) presents the calculated amplitude sensitivity for three different thicknesses: 0.05 μm, 0.1 μm, and 0.15 μm. The amplitude sensitivity is a crucial parameter as it reflects how effectively the sensor can detect changes in the RI of the analyte. At an RI of

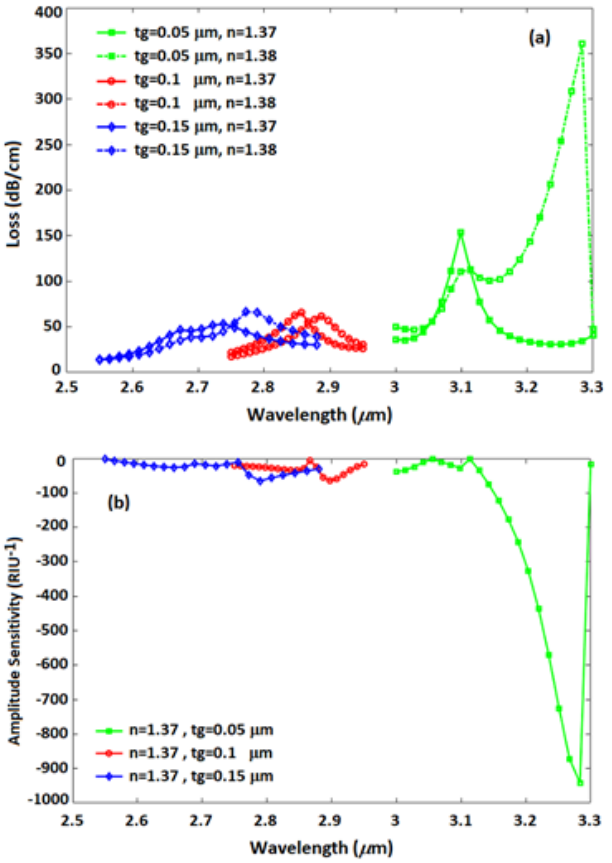

Figure 5. Effect of changes in gold layer thickness on (a) Losses, (b) Amplitude sensitivity.

1.37, the amplitude sensitivity values are determined to be: -950 RIU^{-1}, -90 RIU^{-1}, and -80 RIU^{-1}, respectively. These results clearly indicate that the 0.05 μm thickness provides the highest amplitude sensitivity, making it the optimal choice. This thickness achieves a balance between maintaining high sensitivity and minimizing transmission loss, thereby ensuring the most effective performance for the sensor.

3.2.2 Plasmonic material selection

In PCF-SPR sensors, plasmonic materials such as silver (Ag), gold (Au) and indium tin oxide (ITO) are commonly used due to their real negative dielectric constants, which facilitate effective resonance [34–37]. This section examines the impact of these plasmonic materials on the performance of the C-PCF-SPR sensor with three central air holes. Fig. 6 (a) illustrates the loss spectrum of the sensor at a RI of 1.37, with the plasmonic material layer thicknesses set to 0.05 μm for gold (Au), silver (Ag), and indium tin oxide (ITO). The C-PCF-SPR sensor with a gold plasmonic material demonstrates a broader peak loss compared to those using silver and ITO films. This broader peak indicates a more robust resonance effect, which is crucial for accurate sensing. To further assess the effect of the plasmonic material type on the sensor's functionality, Fig. 6 (b) shows the calculated amplitude sensitivity (SA) of the C-PCF-SPR sensor for each material at a refractive index of 1.3. The amplitude sensitivity values are as follows: Gold (Au): -950 RIU^{-1}, Silver (Ag): -220 RIU^{-1}, Indium Tin Oxide (ITO): -80 RIU^{-1}. These results clearly indicate that gold provides the highest amplitude sensitivity among the three materials. This makes it the most effective material for this sensor design. Gold's superior performance is attributed to its chemical stability and its ability to sustain a broader resonance peak, which enhances the sensor's sensitivity to changes in the refractive index.

3.2.3 Adoption and validation of air hole radius

The optimization process for the structure in our study is based on the comprehensive analysis presented in reference [28]. This reference includes a detailed examination of air hole size variations and their impact on the photonic crystal fiber's dispersion and confinement loss. Given that the design and optimization methodology in [28] is highly detailed and specifically addresses the performance of the photonic crystal fiber (PCF) under study, we have adopted those values as the baseline for our work. Our focus was primarily on leveraging this established design to achieve specific enhancements within our targeted refractive index range. We have concentrated on modifications that do not compromise the optimized parameters while achieving the desired performance improvements in our application.
In order to achieve the desired specifications for this structure in the sensor design, the effect of variations in the air hole radius was examined. The evaluation range for the three central air holes and the other rings was considered

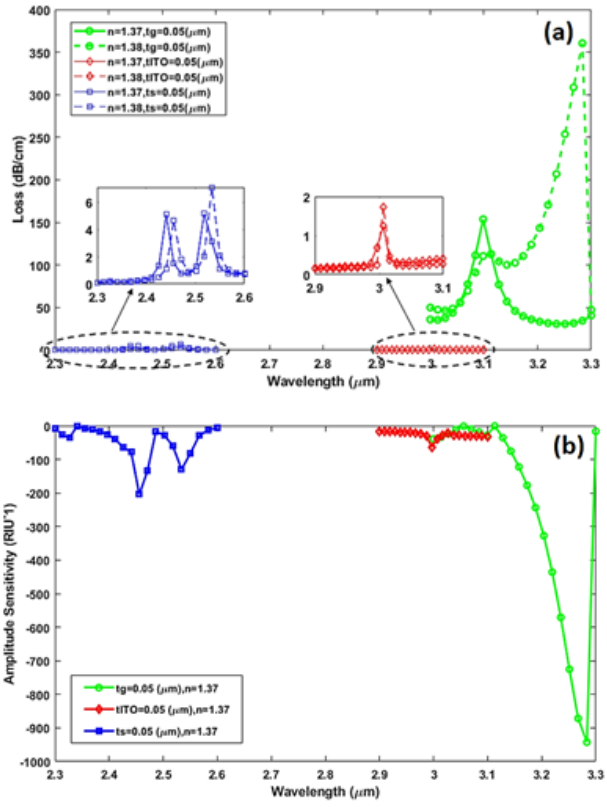

Figure 6. evaluate the impact of variations in the type of plasmonic material on (a) Losses, and (b) Amplitude sensitivity, at the refractive index $n = 1.37$ and the plasmonic material thickness $t_g = t_{ITO} = t_s = 0.05$ um.

between 0.4 and 0.7. After extensive simulations and selecting different values within the desired range, values of 0.7 for the three central air holes and the first ring, as well as 0.4 for the other rings, were obtained as an optimized structure. For the sample, Initial Structure, Modified Structure and Optimal Structure with the following specifications were considered.

In the first structure, the radius of the three central air holes was set to 0.4 μm, while the radius of the other rings was set to 0.7 μm (Fig. 7 (a)). This configuration resulted in a low confinement loss rate, which hindered effective detection. The loss was insufficient to achieve the desired sensitivity, indicating that the initial dimensions were not optimal for enhancing the sensor's performance. To improve the performance, the radius of the air holes in the additional rings was decreased from 0.7 μm to 0.4 μm, while maintaining the radius of the three central air holes fixed at 0.4 μm (Fig. 7 (b)). This modification led to an increase in confinement loss and a shift towards longer wavelengths. Although this was an improvement over the initial structure, it still did not reach optimal performance. For the final structure, the radius of the three central air holes was increased to 0.7 μm, while the radius of the second ring was also set to 0.7 μm. The other rings were simulated with a radius of 0.4 μm (Fig. 7 (c)). This configuration produced a significantly higher and detectable confinement loss rate. The findings suggest that as the air hole radius in the first and second rings increases, there is a corresponding rise in loss. This occurrence is attributed due to the following factors: This phenomenon occurs due to the following factors: Fiber Core Squeezing (Enlarging the air holes in the first and second rings compresses the fiber core, which facilitates more energy coupling into the metal-dielectric interface) and Improved Energy Transfer (The reduction in the radius of the air holes in the third to fifth rings enhances energy transfer, contributing to an increase in the SPR coupling effect).

3.3 RI sensing characteristics of the designed sensor

3.3.1 Amplitude sensitivity (S_A)

The sensor's amplitude sensitivity (S_A), illustrated in Fig. 8, demonstrates a positive correlation with the increasing resonance peak. The peak amplitude sensitivity recorded is 942.4699 RIU^{-1}. This parameter is crucial as it quantifies how much the resonance wavelength shifts in response to the mass of the detected biomolecules. The amplitude sensitivity is given in units of RIU^{-1}, indicating the variation in the resonance wavelength for each unit change in the RI of the analyte. The amplitude sensitivity S_A can be mathematically determined using the following equation [13]:

$$S_A(\lambda)[\mathrm{RIU}^{-1}] = -\frac{1}{\alpha(\lambda n_a)}\frac{\partial\alpha(\lambda n_a)}{\partial n_a} \tag{7}$$

In the equation (7), finite losses associated with the analyte's refractive index has been presented by $\alpha(\lambda n_a)$,. $\partial\alpha(\lambda n_a)$ indicates the difference in finite losses between two consecutive refractive indices of the analyte.

3.3.2 wavelength sensitivity (S_λ)

Wavelength sensitivity is a critical parameter that measures how much the resonance wavelength of the sensor shifts in response to variations in the RI of the surrounding medium. It highlights the proposed device's enhanced ability to detect even more subtle changes in the refractive index (RI), which is essential for accurate sensing applications. The sensitivity in the wavelength interrogation technique, denoted as S_λ,

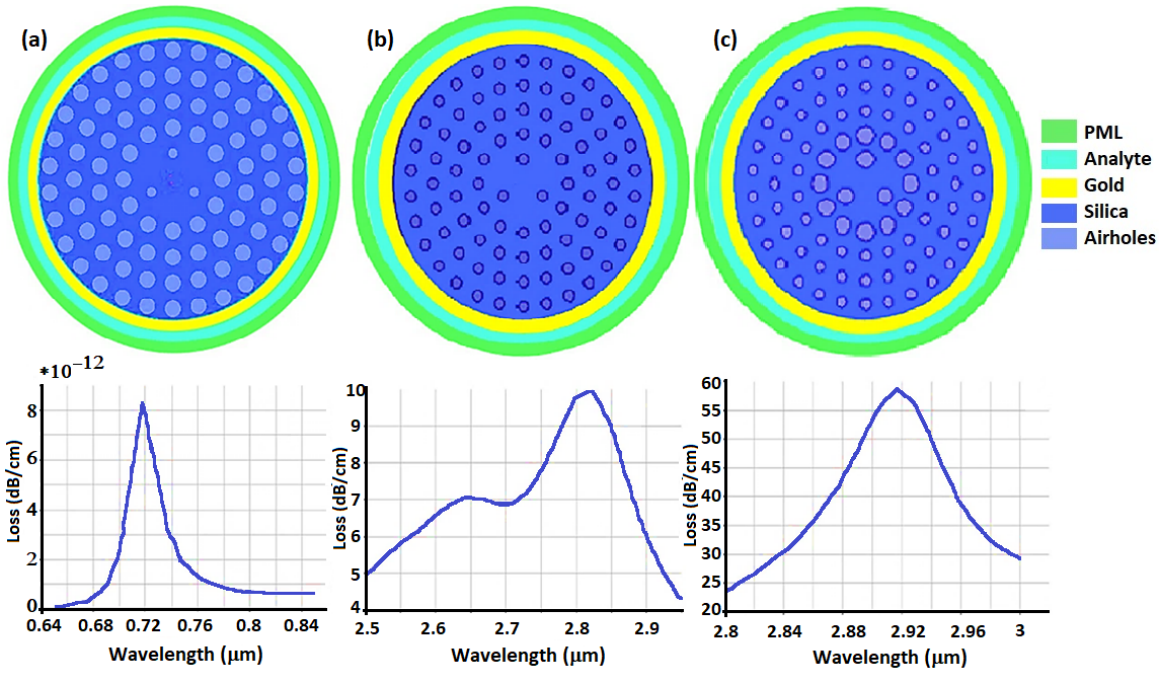

Figure 7. Effect of changes in the air hole diameter in the cold layer on losses, (a) Three central holes with the radius of 0.4 um and other rings with the radius of 0.7 um, (b) three central holes with the radius of 0.4 um and other rings with the radius of 0.4 um, (c) three central holes with the radius of 0.7 um, the second ring with the radius of 0.7 um and other rings with the radius of 0.4 um.

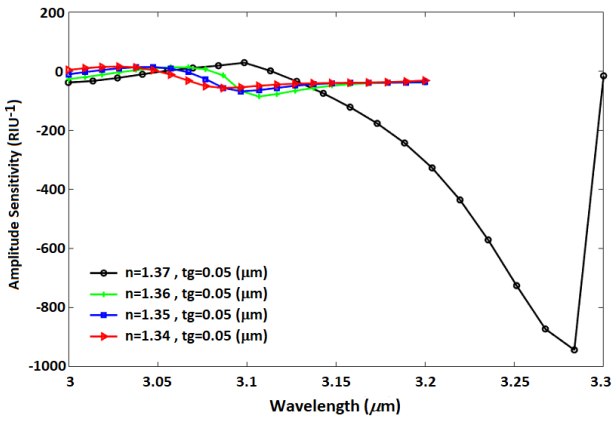

Figure 8. Alterations in amplitude sensitivity resulting from changes in the analyte's refractive index (RI).

can be computed by the equation (7) [13]:

$$S_\lambda(\lambda)[\text{nm/RIU}] = \Delta\lambda_{\text{peak}}/\Delta n_a \tag{8}$$

where $\Delta\lambda_{\text{peak}}$ is the change in resonance wavelength, Δn_a is the change in refractive index.

The amplitude interrogation technique relies on intensity measurements, utilizing the difference between modal losses and the refractive index (RI) of the analyte.

The wavelength sensitivity (S_λ) of the proposed structure has been calculated within a refractive index (RI) range spanning from 1.34 to 1.38. Using the wavelength sensitivity equation (equation (8)) the sensitivities for different RIs are computed as follows: For RI 1.34, 1.35, 1.36 and 1.37 are 977 nm/RIU, 1973 nm/RIU, 995 nm/RIU and 18681 nm/RIU, respectively.

Table 1 reports, the peak loss and resonance wavelength data reveal that the maximum shift in resonance wavelength occurs when the RI changes from 1.37 to 1.38, resulting in a shift of 186.81 nm. Consequently, using the given equation, the sensor's maximum wavelength sensitivity is calculated to be 18681 nm/RIU. This high sensitivity indicates the sensor's exceptional capability in detecting small variations in the refractive index with precise wavelength shifts.

3.3.3 Resolution (R)

The resolution (R) of a sensor is a critical parameter that defines its capacity to identify subtle changes in the refractive index (RI). It is calculated using the following formula:

$$R_\lambda[\text{RIU}] = \Delta n_a \times \Delta\lambda_{\text{min}}/\Delta\lambda_{\text{peak}} \tag{9}$$

where $\Delta\lambda_{\text{min}}$ represents the minimum spectral resolution, and $\Delta\lambda_{\text{peak}}$ indicates the shift in the resonant wavelength peak. In our design structure, the values of various parameters are $\Delta n_a = 0.01$, $\Delta\lambda_{\text{min}} = 0.1$ nm, and $\Delta\lambda_{\text{peak}} = 9.77$ nm. Assuming a minimum detectable intensity change of 1% for accurate detection, the resolution can be further refined. For the proposed sensor, the high-resolution value obtained is: $R_{\text{min}} = 1 \times 10^{-4}$ RIU. This suggests that the sensor is capable of detecting extremely subtle changes in refractive index. It is important to note that the functionality of the proposed structure strongly depends on the evanescent field. A highly intense evanescent field can lead to significant transmission losses, which must be managed to maintain effective sensor operation [36].

3.3.4 length of the sensor (S_L)

The sensor's length (S_L) is adjusted based on the refractive index (RI). It can be computed using the following equation [38].

$$L[\text{cm}] = 1/\alpha(\lambda n_a) \tag{10}$$

In the above equation, $\alpha(\lambda n_a)$ represents the coupling loss (CL) at a specific wavelength and refractive index (RI). Fig. 9 shows that as the refractive index (RI) increases, the sensor length progressively decreases.

3.3.5 Figure of Merit (FOM)

The signal-to-noise ratio (SNR) is a critical factor in evaluating sensor performance. Generally, a higher SNR corre-

Table 1. Performance of the designed sensor in the range of 1.34 to 1.38.

Refractive Index (n_a)	Shift of Δn_a	Resonance Wavelength λ_{peak} (nm)	Peak Shift $\Delta\lambda_{peak}$ (nm)	Confinement Loss (dB/cm)	Resolution R (RIU)	Wavelength Sensitivity S_λ (nm/RIU)	Amplitude sensitivity S_A RIU^{-1}	Sensor Length (cm)	FWHM (nm)	FOM (RIU^{-1})
1.34	0.01	3057.32	9.77	64.48	1×10^{-4}	977	-80	0.0155	97.4	10.03
1.35	0.01	3067.09	19.73	79.3355	5×10^{-5}	1973	-90	0.0126	80	24.6625
1.36	0.01	3086.82	9.95	104.109	1×10^{-4}	995	-100	0.0096	60	16.5833
1.37	0.01	3096.77	186.81	152.512	53×10^{-7}	18681	-950	0.0063	60	311.35
1.38	0.01	3283.58	-	360.386	-	-	-	0.0027	80	-

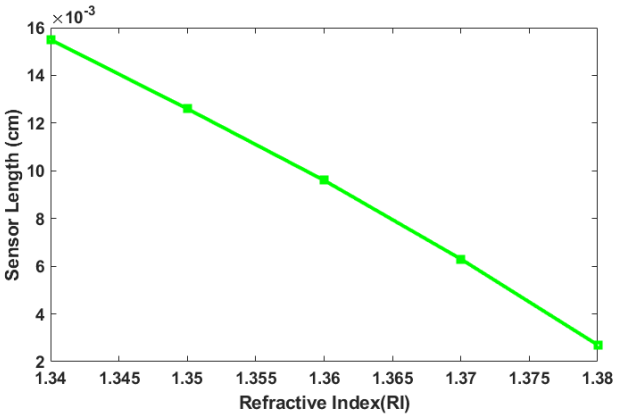

Figure 9. Changing of sensor length (cm) with different values of RI.

sponds to a smaller standard deviation in spectral variations, resulting in better detection performance Improvements in spectral width and SNR result in an elevated detection limit, which can be quantified using the Figure of Merit (FOM). The FOM provides a crucial metric for evaluating the sensor's performance and can be computed by the equation (11) [38]:

$$\mathrm{FOM}[\mathrm{RIU}^{-1}] = S_\lambda\,(\mathrm{nm/RIU})/\mathrm{FWHM(nm)} \qquad (11)$$

In this context, sensitivity is characterized by the shift in resonance wavelength for each unit change in the refractive index. The Full Width at Half Maximum (FWHM) is the width of the resonance peak measured at half of its maximum intensity. The Figure of Merit (FOM) is then calculated by dividing the sensitivity by the FWHM. This ratio provides a measure of how effectively the sensor can discriminate between different refractive indices, with a higher FOM indicating better performance.

3.3.6 Fitting result

The correlation between shifts in the resonance wavelength and changes in the analyte's refractive index (RI) has been shown in Fig. 10. The plotted curves demonstrate a strong linear correlation, with a high R^2 value of 0.98, indicating excellent fit. The linear equation describing this relationship is y = 1380.8X + 1206. This linear behavior within the RI range of 1.34 to 1.37 is advantageous for the practical calibration of the sensor, facilitating straightforward and accurate adjustments before testing with actual analytes.

Table 2 compares the proposed sensor with the previous structures. The design presented in [9], which incorporates internal sensing capability and two gold-filled air holes, demonstrates a wavelength sensitivity that is 4.5 times lower and an amplitude sensitivity that is 1.12 times higher compared to our sensor. This internal sensing design poses significant manufacturing challenges, especially with the difficulty of filling the air holes with gold. In contrast, our suggested design with the ability of external sensing not only simplifies the manufacturing process but also provides significantly higher maximum wavelength sensitivity compared to the structure from [9], while achieving comparable maximum amplitude sensitivity.

The maximum amplitude sensitivity of the structure presented in [14], which features external sensing capability, is 2.3 times lower than that of our sensor. A significant challenge with this structure is its complex manufacturing process, which involves a specialized arrangement of air holes and the difficulty of converting a PCF with five rings of air holes into this configuration. In contrast, our proposed C-PCF-SPR sensor, which retains a design similar to the original PCF and also employs external sensing capability, simplifies the manufacturing process while achieving significantly higher maximum amplitude sensitivity. Although the maximum wavelength sensitivity of the proposed C-PCF-SPR sensor is lower compared to the structure from [14], its considerable wavelength sensitivity, combined with easier manufacturing and higher overall efficiency, makes it a more practical and effective choice.

A quasi-D-shaped sensor which has been presented in [18] shows maximum amplitude and wavelength sensitivities that are 2 and 4.5 times lower, respectively, compared to those of the proposed C-PCF-SPR sensor. In 2020, the sensor which has been described in [15] has maximum amplitude and wavelength sensitivities that are 63 and 1.8 times lower, respectively, than those of our sensor. Additionally, in the year of 2019 the sensor has been presented which has a maximum wavelength sensitivity that is 2.4 times lower than that of the C-PCF-SPR sensor with three central air holes, though its amplitude sensitivity was not provided [5]. The sensor presented in 2021 [13] exhibits higher maximum amplitude and wavelength sensitivities compared to our C-PCF-SPR sensor. However, it requires a more intricate manufacturing process because of the need to remove the air hole rings and the creation of six additional air holes in its structure. In contrast, the C-PCF-SPR sensor with three central air holes and external sensing capability, which closely resembles the original photonic crystal fiber design, addresses the manufacturing challenges effectively. It achieves significant maximum wavelength and amplitude sensitivities, surpassing those of previously reported sensors, particularly within the refractive index range of $1.34 - 1.38$.

Thus, the highly sensitive C-PCF-SPR sensor is highly efficient for detecting harmful bacteria or pests in air, water, or

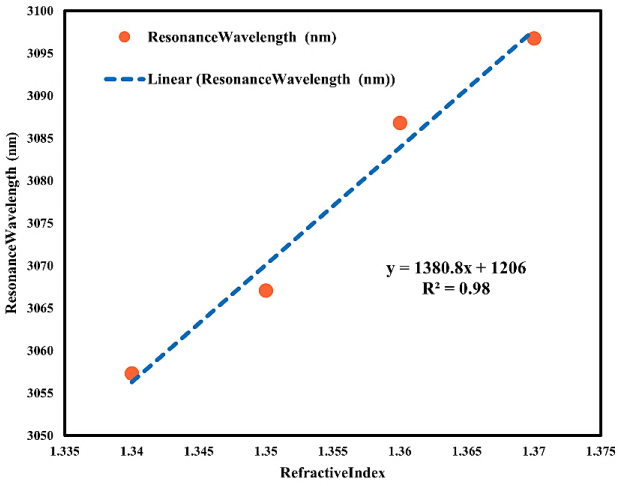

Figure 10. Fitting results between resonance wavelength and RI.

Table 2. Comparing the C-PCF-SPR sensor with three central air holes with previous structures.

PCF-SPR Design Refs.	Key Features	Fabrication complexity	Plasmonic material	RI Range	Max. Wavelength Sensitivity (nm/RIU)	Max. amplitude sensitivity (RIU^{-1})	Schematics design
Guangyao Wang et al. (2020) [9]	Gold-filled air holes, high complexity, limited RI range	High (Gold filled air holes)	Gold	1.29 – 1.49	−4156.82	−1056.33	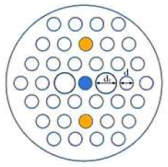
K.M. Mustafizur Rahman et al. (2021) [14]	Alternative plasmonic material (ITO), broad wavelength sensitivity	Medium (ITO deposition)	ITO	1.33 – 1.4	37000	−407.285	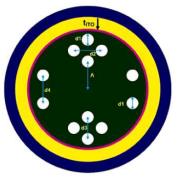
Hongyan Yang et al. (2021) [18]	Hybrid design with graphene and gold, high fabrication complexity	High (Hybrid graphene-gold)	graphene-Au	1.32 – 1.41	4200	−450	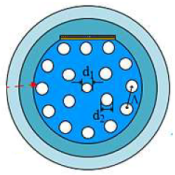
Veerpal Kaur et al. (2020) [15]	Dual-layer plasmonic material (ITO/ZnO), moderate sensitivity	Medium (Dual oxide layers)	ITO/ZnO	1.30 – 1.38	10000	−15	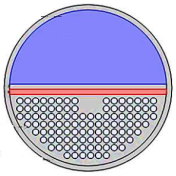
Suoda Chu et al. (2019) [5]	D-shaped configuration, moderate sensitivity	Medium (D-shaped design)	Gold	1.33 – 1.41	7900	-_	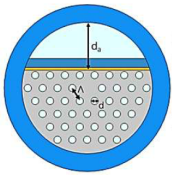
Mohammad Rakibul Islam et al. (2021) [13]	High sensitivity, complex structure with multiple layers	High (Multiple layers, structural modifications)	Gold	1.33 – 1.39	32000	−1757.3	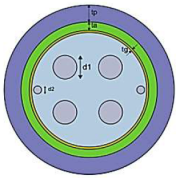
Proposed Structure	Simplified fabrication external sensing, competitive sensitivity and resolution ,	Low (Simple external coating)	Gold	1.34 – 1.38	18681	−942.4699	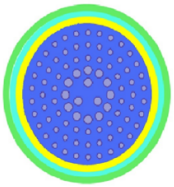

food, making it a valuable tool for anti-bioterrorism applications. Additionally, it can be employed in chemical and biological warfare scenarios to detect and avoid exposure to hazardous chemical gases and infections. The sensor's versatility also extends to small-scale and portable devices, enabling users to monitor vital signs, manage disorders, and detect critical signals in emergency situations.

Currently, many diagnostic tests such as the Coombs test, blood count, biopsy, and blood sugar test are used to examine human disorders and diagnose cancer. These conventional methods are often time-consuming, painful, and require expensive equipment. In contrast, the C-PCF-SPR sensor, which operates within the refractive index (RI) range of 1.34 – 1.38, offers a more cost-effective and efficient alternative. This sensor is particularly adept at detecting various blood components, including plasma (RI of 1.35), white blood cells (WBC) (RI of 1.36), hemoglobin (Hb) (RI of 1.38), ethanol (RI of 1.36), and kiptone (RI of 1.34) [20–23].

MDA-MB-231 cells are a specific type of breast cancer

cell. Traditional breast examination methods, such as X-ray mammograms, typically detect tumors only after they have grown three to four times their original size and metastasized. However, a novel blood test has been recently proposed that can diagnose breast cancer when the tumor is still as small as a seed, even before any symptoms appear. The simulated sensor discussed in this paper, featuring a gold layer thickness of 0.1 μm, demonstrates the potential to detect extremely small changes in the refractive index (RI) of cells. This high sensitivity enables the sensor to distinguish between cancerous and healthy cells by identifying RI differences down to the hundredth order of magnitude. Such precision not only facilitates the early detection of cancer but also allows for continuous monitoring of cancer progression by tracking gradual RI changes in cells. This makes the sensor an invaluable tool for both early detection and precise diagnosis of cancer.

As illustrated in Fig. 11, the detectable refractive index (RI) range for the C-PCF-SPR sensor with three central air holes is from 1.33 to 1.45, with a gold layer thickness of t_g = 0.1 μm. The mean RIs of healthy cells typically fall between 1.35 and 1.37, whereas cancerous cells exhibit slightly higher RIs, ranging from 1.39 to 1.40. This difference in RI is due to the higher protein content in the nuclei of cancer cells, which is essential for their rapid reproduction. Consequently, this RI disparity allows for straightforward differentiation between healthy and cancerous cells using the sensor.

As cancer progresses, the target cells' RI increases further, leading to greater shifts in resonance wavelengths. By monitoring these shifts, the progression of the disease can be tracked over time, providing valuable insights into the stage and advancement of cancer. This capability highlights the sensor's potential for early detection and monitoring of cancerous cells based on their RI characteristics.

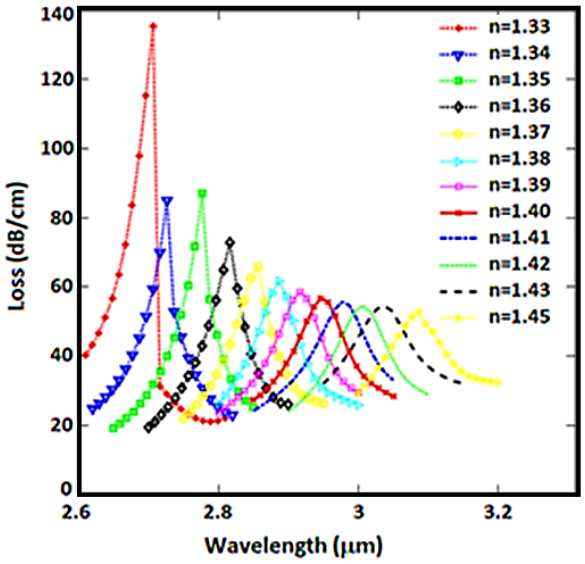

Figure 11. Loss spectrum of C-PCF-SPR for analyte RI varying from 1.33 to 1.45 at t_g = 0.1 um to distinguish healthy cells from cancer cells.

4. Conclusion

This work introduces a novel gold-coated circular photonic crystal fiber surface plasmon resonance (C-PCF-SPR) sensor that balances high sensitivity with a simplified fabrication process. Our design achieves maximum wavelength and amplitude sensitivities of 18681 nm/RIU and 942.47 RIU^{-1}, respectively, within the refractive index range of $1.34 - 1.38$. Compared to previously reported designs, the proposed sensor offers competitive performance while minimizing manufacturing complexities. These features make it suitable for a wide range of applications, including biochemical sensing and early cancer detection. Future work will focus on extending the sensor's operational range by incorporating alternative plasmonic materials and exploring hybrid configurations to enhance detection capabilities further.

Acknowledgements

This article has been previously published as a preprint in the research square (ResearchGate) (DOI: 10.21203/rs.3.rs-3356667/v1).

Authors contributions

Maryam Mirasanloo Zeydi performed conceptualization, methodology, software, validation, formal analysis, investigation, resources, writing original draft, and visualization. Seyed Saleh Ghoreishi Amiri provided conceptualization, methodology, investigation, resources, writing-review & editing, and supervision. Reza Yousefi analyzed conceptualization, methodology, investigation, writing-review & editing, and supervision. Habib Adarang presented conceptualization, methodology, investigation, writing-review & editing, and supervision.

Availability of data and materials

The authors declare that the data supporting the findings of this study are available within the paper.

Conflict of interests

The authors assert that they do not have any identifiable conflicting financial interests or personal relationships that might be perceived to influence the work presented in this paper.

References

[1] B. Liedberg, I. Lundström, and E. Stenberg. "Principles of biosensing with an extended coupling matrix and surface plasmon resonance.". *Sensors and Actuators B: Chemical*, 11((1-3)):63–72, 1993. DOI: https://doi.org/10.1016/0925-4005(93)85239-7.

[2] B. Sadeghi, S. H. Ghammamy, Z. Gholipour, M. Ghorchibeigy, and A. A. Nia. "Gold/hydroxypropyl cellulose hybrid nanocomposite constructed with more complete coverage of gold nano-shell.". *Micro and Nano Letters*, 6(4):209–213, 2011. DOI: https://doi.org/10.1049/mnl.2011.0036.

[3] A. Amininia, K. Pourshamsian, and B. Sadeghi. "Nano-ZnO Impregnated on Starch-A Highly Efficient Heterogeneous Bio-Based Catalyst for One-Pot Synthesis of Pyranopyrimidinone and Xanthene Derivatives as Potential Antibacterial Agents.". *Russian Journal of Organic Chemistry*, 56(7):1279–1288, 2020. DOI: https://doi.org/10.1134/S1070428020070234.

[4] K. Matsubara, S. Kawata, and S. Minami. "Optical chemical sensor based on surface plasmon measurement.". *Applied Optics*, 27(6): 1160, 1988. DOI: https://doi.org/10.1364/ao.27.001160.

[5] S. Chu, K. Nakkeeran, S. Member, A. M. Abobaker, S. S. Aphale, S. Member, S. Sivabalan, P. R. Babu, and K. Senthilnathan. "Influence of the Sub-peak of Secondary Surface Plasmon Resonance onto the Sensing Performance of a D-shaped Photonic Crystal Fibre Sensor.". *IEEE Sensors Journal*, 1, 2019.
DOI: https://doi.org/10.1109/JSEN.2019.2953393.

[6] S. Mittal, A. Saharia, Y. Ismail, F. Petruccione, A. V. Bourdine, O. G. Morozov, V. V. Demidov, J. Yin, G. Singh, M. Tiwari, and S. Kumar. "Design and Performance Analysis of a Novel Hoop-Cut SPR-PCF Sensor for High Sensitivity and Broad Range Sensing Applications.". *IEEE Sensors Journal*, 24(3), 2024.
DOI: https://doi.org/10.1109/JSEN.2023.3339813.

[7] K. Ahmed, R. Amin, F. M. Bui, L. Chen, N. Mohammadd, F. A. Al-Zahrani, and S. Kumar. "Design and Analysis of Multi-Analyte Detection Based Biosensor in the Visible to Near-Infrared (VNIR) Region.". *IEEE Transactions on Nanobioscience*, 23(1), 2024.
DOI: https://doi.org/10.1109/TNB.2023.3281527.

[8] S. Das and R. Sen. "Design and Numerical Analysis of a PCF-SPR Sensor for Early-stage Malaria Detection.". *Plasmonics*, 2024.
DOI: https://doi.org/10.1007/s11468-024-02193-9.

[9] G. Wang, Y. Lu, L. Duan, and J. Yao. "A refractive index sensor based on PCF with ultra-wide detection range.". *IEEE Photonics Journal*, 27, 2020.
DOI: https://doi.org/10.1109/JSTQE.2020.2993866.

[10] W. Liu. "A hollow dual-core PCF-SPR sensor with gold layers on the inner and outer surfaces of the thin cladding.". *Results in Optics*, 1:100004, 2020.
DOI: https://doi.org/10.1016/j.rio.2020.100004.

[11] V. Kaur and S. Singh. "Design of titanium nitride coated PCF-SPR sensor for liquid sensing applications.". *Optical Fiber Technology*, 48:159–164, 2019.
DOI: https://doi.org/10.1016/j.yofte.2018.12.015.

[12] M. R. Islam, A. Jamil, S. Asir, H. Ahsan, M. K. Pulak, F. Mehjabin, M. I. Khan, J. A. Chowdhury, and M. Isla. "Design and Analysis of Birefringent SPR Based PCF Biosensor with Ultra-High Sensitivity and Low Loss Mohammad.". *Optik - International Journal for Light and Electron Optics*, page 165311, 2020.
DOI: https://doi.org/10.1016/j.ijleo.2020.165311.

[13] M. R. Islam. "Design and numerical analysis of a gold-coated photonic crystal fiber based refractive index sensor.". *Optical and Quantum Electronics*, 53, 2021.
DOI: https://doi.org/10.1007/s11082-021-02748-8.

[14] K. M. M. Rahman, M. S. Alam, R. Ahmed, and M. A. Islam. "Results in Physics Irregular hexagonal core based surface plasmon resonance sensor in near-infrared region. ". *Results in Physics*, 23:103983, 2021.
DOI: https://doi.org/10.1016/j.rinp.2021.103983.

[15] V. Kaur and S. Singh. "Design of D-Shaped PCF-SPR sensor with dual coating of ITO and ZnO conducting metal oxide.". *Optik*, 220: 165135, 2020.
DOI: https://doi.org/10.1016/j.ijleo.2020.165135.

[16] S. Singh and Y. K. Prajapati. "Optik TiO_2 / gold-graphene hybrid solid core SPR based PCF RI sensor for sensitivity enhancement.". *Optik*, 224:165525, 2020.
DOI: https://doi.org/10.1016/j.ijleo.2020.165525.

[17] Y. Esfahani Monfared. "Refractive index sensor based on surface plasmon resonance excitation in a D-shaped photonic crystal fiber coated by titanium nitride.". *Plasmonics*, 15:535–542, 2020.
DOI: https://doi.org/10.1007/s11468-019-01072-y.

[18] H. Sensitive and G. C. Plasmon. "Highly Sensitive Graphene-Au Coated Plasmon Resonance PCF Sensor.". *Sensors*, 21, 2021.
DOI: https://doi.org/10.3390/s21030818.

[19] A. Noman, Member G. S. Al, A. Hossain, and S. Member. "Highly Sensitive D-Shaped Plasmonic Refractive Index Sensor for a Broad Range of Refractive Index Detection.". *IEEE Photonics*, 13, 2021.
DOI: https://doi.org/10.1109/JPHOT.2021.3055234.

[20] H. Sharifi and S. Eskandari. "Sensing blood components and cancer cells with photonic crystal resonator biosensor.". *Results in Optics*, 14, 2024.
DOI: https://doi.org/10.1016/j.rio.2023.100593.

[21] M. K. Khalaf, H. J. Taher, S. R. Tahhan, K. Ahmed, and F. A. Al-Zahrani. "Design and Numerical Analysis of Refractive Index-Based Reproductive Hormone Sensor.". *Plasmonics*, 2024.
DOI: https://doi.org/10.1007/s11468-024-02208-5.

[22] W. Qu, Y. Chen, C. Ma, D. Peng, X. Bai, J. Zhao, S. Liu, and L. Luo. "Application of Optical Fiber Sensing Technology and Coating Technology in Blood Component Detection and Monitoring.". *Coatings*, 14, 2024.
DOI: https://doi.org/10.3390/coatings14020173.

[23] Z. Du and H. Liu. "Elliptical photonic crystal fiber sensor for multi-function detection based on surface plasmon resonance.". *Indian Journal of Physics*, 98(1), 2024.
DOI: https://doi.org/10.1007/s12648-023-02791-z.

[24] M. R. Sardar and M. Faisal. "Dual-Core Dual-Polished PCF-SPR Sensor for Cancer Cell Detection.". *IEEE Sensors Journal*, 24(7), 2024.
DOI: https://doi.org/10.1109/JSEN.2024.3358173.

[25] M. Fazeli. "Design and Simulation of Photonic Crystal Fiber Based Surface Plasmon Resonance Biosensor for Cancer Diagnosis.". 2021.
DOI: https://doi.org/10.21203/rs.3.rs-397327/v1.

[26] S. Jain, K. Choudhary, A. Kumar, C. Marques, and S. Kumar. "PCF-based plasmonic sensor for the detection of cervical and skin cancer cell.". *Results in Optics*, 14, 2024.
DOI: https://doi.org/10.1016/j.rio.2023.100589.

[27] F. yuanyuan, X. Tengfei, C. Desheng, Q. Kai, and P. Shengli. "Design and Analysis of Surface Plasmon Resonance Sensor with Open-Loop Side-Polished Photonic Crystal Fiber.". *plasmonics*, 2024.
DOI: https://doi.org/10.1007/s11468-024-02292-7.

[28] G. D. Krishna, V. P. M. Pillai, and K. G. Gopchandran. "Design of low dispersion and low loss photonic crystal fiber: Defected core circular-octagon hybrid lattices.". *Optical Fiber Technology*, 51: 17–24, 2019.
DOI: https://doi.org/10.1016/j.yofte.2019.04.015.

[29] L.-Q. Chen, Y.-C. Wu, Y. Liu, H. Y. Cai, and J. Liu. "Highly sensitive dual-function sensor for refractive index and temperature using D-shaped microchannel photonic crystal fiber.". *Optics Express*, 32(7), 2024.
DOI: https://doi.org/10.1364/oe.519749.

[30] X. Yang, Y. Lu, B. Liu, and J. Yao. "Analysis of graphene-based photonic crystal fiber sensor using birefringence and surface plasmon resonance.". *Plasmonics*, 12:489–496, 2017.
DOI: https://doi.org/10.1007/s11468-016-0289-z.

[31] H. Search, C. Journals, A. Contact, M. Iopscience, and I. P. Address. "A new design of photonic crystal fiber with ultra-flattened dispersion to simultaneously minimize the dispersion and confinement loss.". *Journal of Physics*, 2011.
DOI: https://doi.org/10.1088/1742-6596/276/1/012080.

[32] S. O. F. Taghipour. "Ultra-flattened dispersion hexagonal photonic crystal fibre with low confinement loss and large effective area.". *IET Optoelectronics*, 6:82–87, 2012.
DOI: https://doi.org/10.1049/iet-opt.2011.0031.

[33] S. Mohammadnejad. "Novel Design to Compensate Dispersion for Index-Guiding Photonic Crystal Fiber with Defected Core.". *2010 2nd International Conference on Mechanical and Electronics Engineering*, pages 417–421, 2010.
DOI: https://doi.org/10.1109/ICMEE.2010.5558394.

[34] M. R. Islam, A. N. M. Iftekher, M. Ehsanul Haque, S. Tasnim, and R. R. Karim. "Double Polarization Peak Shift Sensitivity : An interrogation technique for a PCF SPR sensor.". *Optik*, 299, 2024. DOI: https://doi.org/10.1016/j.ijleo.2024.171617.

[35] H. Pan, N. Cui, and B. Zhang. "High Sensitivity Surface Plasmon Resonance Sensor Based on ITO-Coated Photonic Crystal Fiber with Simple Structure.". 2022. DOI: https://doi.org/10.21203/rs.3.rs-2216102/v1.

[36] A. M. T. Hoque, K. F. Al-Tabatabaie, M. E. Ali, A. M. Butt, S. S. I. Mitu, and K. K. Qureshi. "U-Grooved Selectively Coated and Highly Sensitive PCF-SPR Sensor for Broad Range Analyte RI Detection.". *IEEE Access*, 11, 2023. DOI: https://doi.org/10.1109/ACCESS.2023.3261565.

[37] J. Divya, S. Selvendran, A. S. Raja, and V. Borra. "A Novel Plasmonic Sensor Based on Dual-Channel D-Shaped Photonic Crystal Fiber for Enhanced Sensitivity in Simultaneous Detection of Different Analytes.". *IEEE Transactions on Nanobioscience*, 23(1), 2024. DOI: https://doi.org/10.1109/TNB.2023.3294330.

[38] N. Slam, M. Faizul Huq Arif, M. Abu Yousuf, and S. Asaduzzaman. "Highly sensitive open channel based PCF-SPR sensor for analyte refractive index sensing.". *Results in Physics*, 46:106266, 2023. DOI: https://doi.org/10.1016/j.rinp.2023.106266.